LINKING MINERAL REACTIVE SURFACE AREA WITH ITS DISTRIBUTION AND PORE GEOMETRY

Ma Jin[1], Duncan Webster[2], Xiang-Zhao Kong[1*], Martin O. Saar[1]
[1]Geothermal Energy & Geofluids Group, Department of Earth Sciences, ETH-Zürich, CH-8092, Switzerland, [2]SCANCO Medical, Bruettisellen Switzerland

This paper was prepared for presentation at the International Symposium of the Society of Core Analysts held in Vienna, Austria, 27 August – 1 September 2017

ABSTRACT

Fluid-rock interactions play an important role in geological and geo-engineering processes, such as chemical stimulation of enhanced geothermal systems and carbon capture, utilization, and storage (CCUS). However, involved reactions are highly dependent on the accessible reactive surface area of minerals which is difficult to quantify. In particular, it is difficult to quantify the surface area of each reacting mineral within whole rock samples, due to the typically heterogeneous distribution of minerals and pores. In this study, we perform detailed laboratory analyses on sandstone samples from deep geothermal sites in Lithuania, in an effort to better quantify reactive surface areas.

We measure specific surface area (SSA) of whole rock samples using a gas adsorption method (BET) with N_2 at a temperature of 77.3 K. We also quantify the samples' porosity and pore size distribution (PSD), using Helium gas pycnometry and Hg porosimetry, respectively. Rock compositions are determined by a combination of X-ray fluorescence (XRF) and quantitative scanning electron microscopy (SEM) - Energy-dispersive X-ray spectroscopy (EDS), which are later geometrically mapped onto 2D images, derived from SEM- Backscattered electrons (BSE, resolution:1.2 µm) and 3D images derived from Micro Computed Tomography (Resolution of 9.5 µm). These digital-mineral maps are then correlated with BET-determined SSA as well as whole-rock porosity and PSD. Porosity and PSD are also analyzed using both 2D and 3D images. It is anticipated that these analyses will provide an in-depth understanding of rock sample chemistry for subsequent hydrothermal-reactive-flow-through experiments on whole-rock samples at elevated pressures and temperatures.

1. INTRODUCTION

Fluid-rock reaction is an important process involved in many geological and geo-engineering systems such as enhanced geothermal systems (EGS) (Althaus and Edmunds, 1987; Pandey et al., 2015) and carbon capture, utilization, and storage (CCUS) (Xu et al., 2003; Guas, 2010). These reactions lead to mineral dissolution and precipitation which may cause changes of reservoir porosity and permeability (Cai et al., 2009; Nogues et al., 2013). Unfavorable fluid-rock reactions can make sustainable reservoir operations challenging. For example, mineral precipitation can lead to a dramatic reduction of the reservoir permeability by several orders of magnitude (Cheshire et al., 2017; Yasuhara et al., 2017) and, consequently, a significant decrease in reservoir productivity/injectivity

during EGS and CCUS. On the other hand, favorable fluid-rock reactions can increase the reservoir permeability by dissolving minerals. For CCUS, such dissolution reactions could facilitate long-term CO_2 mineral trapping (Voskov et al., 2017). However, an increase in reservoir permeability could also cause fluid-pathway "short-circuiting" and lower heat exchange efficiencies in geothermal reservoirs (Feng et al., 2016).

Due to the complexity of coupled fluid flow and fluid-rock reactions, it is well recognized that reactive transport modelling is a powerful approach to predict reservoir operation performances (Beckingham et al., 2016). However, the accuracy of these models depends on reliable measurements of mineral geochemical parameters, among which mineral reactive surface area is the critical one, as it is often poorly constrained in a multi-mineral system (Bourg et al., 2015).

In this study, reactive surface area of individual minerals in sandstone samples is determined by a series of laboratory analyses. A combined method of X-ray fluorescence (XRF), powder X-ray diffraction (XRD), and scanning electron microscope (SEM) - energy dispersive X-ray spectroscopy (EDS) was employed to identify rock compositions. High-resolution SEM - backscatter electron detector (BSE) and SEM-EDS images were analysed to estimate porosity and pore-size distribution (PSD), which were also measured and confirmed by Helium gas pycnometry and mercury porosimetry, respectively. Furthermore, mineral distributions were digitally mapped and reactive surface area of individual minerals was determined. The calculated surface areas were then calibrated, using roughness correction and normalization, to the measurements employing the BET gas absorption method. We also perform 3D micro-CT imaging of a whole-core sample for further analyses of pore connectivity, porosity, and PSD.

2. MATERIALS AND METHODS

2.1 Rock samples

The rock samples used in this study are sandstone, from a depth of 954.6 m in a geothermal well, Vydmantai-1, at the southeast end of the Baltic Sea of Lithuania. The Vydmantai-1 well was drilled in 1989 to a depth of 2564 m (Rasteniene et al, 2005). Transmitted light microscopy observations show that these sandstone samples are well-rounded, fine to very fine grains (sizes of 65μm - 250μm), composed of quartz, feldspar, mica, and a carbonate mineral.

Sandstone specimens were prepared as cylinders, thin sections, and chips for various analyses (see also Sections 2.2 and 2.3). A cylindrical rock specimen with a diameter of 25.4 mm and a length of 39.0 mm was cut for 3D micro-CT imaging, porosity measurements. Later, we will conduct reactive flow-through experiments with the rock cores. A 35 μm-thick thin section with a size of 11.37 mm x 8.34 mm was sliced for microscopy measurements, such as SEM-BSE imaging and SEM-EDS element mapping.

2.2 Porosity and pore size distribution (PSD)

The pore volume of the cylindrical specimen was measured using the Micromeritics AccuPyc II 1340 Pycnometer in the Rock Deformation Laboratory at ETH Zurich. The pore volume was confirmed after 16 purges of Helium at a temperature of 25.14°C. Then

the specimen porosity was obtained as the ratio between the measured pore volume and the total specimen volume. Pore (or throat) size distribution was obtained by Mercury intrusion porosimetry. This PSD measurement was carried out at a temperature of 22.6°C and a maximum pressure of 400 MPa using the Porotec Pascal 140 and 440 (with a detectable size range of 2 nm-100 μm in diameter) in the IGT Claylab at ETH Zurich.

Independent analysis of porosity and PSD of the 35 μm-thick thin section was also performed using various image-processing techniques. The thin section was continuously scanned in 10 x 10 windows using a Jeol JSM-6390 LA SEM together with a BSE in the Electron Microscopy Lab at ETH Zurich. The scanning was performed at an electron accelerating voltage of 15 keV at a working distance of 10 mm to obtain a 1.2 μm-resolution. These 10 x 10 grayscale SEM-BSE coherent images were then stitched using ImageJ to generate a full image of 9474 x 6947 pixel^2, as shown in Figure 1a. Figure 1b shows the corresponding binary image (pores in black and solid in white) using a threshold of 70 on a scale of 0 to 255 (black to white, see the inset with a gray-scale histogram at the top right). This binary image was then used for porosity, PSD, and SSA analyses (see Section 2.4). According to the principle of stereology (Weibel, 1969), the 2D area density mm^2/mm^2 is equivalent to the 3D volume density mm^3/mm^3. The sample porosity can thus be approximated by the 2D areal density mm^2/mm^2 and obtained using image processing. PSD was analysed using the Xlib plugin of ImageJ with a continuous PSD calculation. Its basic principle is that pore space is segmented and measured with circles.

Micro-computed tomography was employed to obtain a 3D geometric representation of the core sample, performed by Scanco Medical AG, Brüttisellen. Cross-section images with 9.5 μm-resolution were acquired using energy of 130 kV and a current of 61 μA. The number of projections was 2000 and the integration time was 3.74 s. Collected images were reconstructed and PSD was analysed using Scanco Medical's Proprietary software (Hilderbrand et al, 1997).

2.3 Mineralogy analysis

Rock compositions were determined using a combination of different techniques, including XRF, XRD, SEM element mapping, and SEM quantitative chemical analysis. To ensure representative measurements, 24.4 g of the sandstone sample was crushed into fine powder for both XRF and XRD analyses.

The XRF analysis was performed using an XRF spectrometer (WD-XRF, PANalytical AXIOS) in the high-pressure Lab at ETH Zurich. During the XRF measurement, 1.5 g of the crushed powder was mixed with Lithium-Tetraborate at a ratio of 1:5 using a Claisse M4® fluxer. The mixture was processed for loss on ignition (LOI) at 1050°C for 2 hours and then melted at 1080°C using the PANalytical Eagon 2 fusion instrument. Weight percentages of 10 major oxides (SiO_2, TiO_2, Al_2O_3, Fe_2O_3, MnO, MgO, CaO, Na_2O, K_2O, P_2O_5) and of 21 trace elements (S, Sc, V, Cr, Co, Ni, Cu, Zn, Ga, Rb, Sr, Y, Zr, Nb, Ba, La, Ce, Nd, Pb, Th, U) were measured during the XRF test. The results were calibrated with ca. 30 certified international standards with emphasis on igneous and metamorphic rock compositions.

The XRD analysis was performed with a Powder X-ray Diffractometer (Bruker AXS D8 Advance) and a Lynxeye superspeed detector in the high-pressure lab at ETH Zurich. The spectrum was analysed using ICDD PDF-2 (Version 4.15.3.4) with the Database Version 2.1502. Crystalline mineral phases were identified as quartz, dolomite, K-feldspar (orthoclase), muscovite, kaolinite and ilmanite. However, XRD analysis is semi-quantitative. To obtain quantitative mineral composition in weight percentage, we need to combine the XRD-XRF results. Taking typical densities of identified minerals (The engineering toolbox: http://www.engineeringtoolbox.com/mineral-density-d_1555.html), we summarize mineral volume fractions in Table 1. Here mineral chemical formulas were confirmed with both XRD and quantitative SEM analysis.

The quantitative SEM analysis was carried out with the Jeol JSM-6390 LA SEM and a EDS system, Thermo Fisher NORAN NSS7, in the high-pressure lab. Elements were mapped on the SEM image with a pixel resolution of 2.4 μm using a 30 mm^2 Silicon-drift detector (SDD). The element-wise pixels were registered according to element X-ray spectra at 20 sec x 50 frames (1000 counts). Similarly, the same area of the thin section as the BSE analysis (11.37mm x 8.34 mm) was continuously scanned with 5 x 5 windows. The resultant 25 coherent images were again stitched using ImageJ to produce a full image of 4737 x 3474 $pixel^2$, as shown in Figure 2. We then overlay all element images to generate a combined SEM-EDS image of mineral distribution. To estimate the chemical formula of individual minerals, we calibrated the X-ray beam current using a Farady-cup, determined element ratios on several spots, and integrated the previous XRD results to produce an average chemical formula, as summarized in Table 1.

2.4 Surface area analysis

Mass-specific surface areas (SSA) of rock samples were measured using a gas adsorption method based on the Brunauer–Emmett–Teller (BET) theory. The measurements were conducted using a surface area analyser, Quantachrome Autosorb 1MP, in the Claylab at ETH Zurich. Before BET measurements, small pieces of rock samples (in total 3.6 g) were vacuumed at 150°C for about 15 hours. During the BET measurements, we employed a 5-point method and nitrogen as the adsorption gas at a temperature of 77.3 K.

Perimeter density ($\mu m/\mu m^2$) in thin section, i.e., the ratio between solid perimeter and solid area, was also independently obtained from the binary image (from the 1.2 μm SEM-BSE image) shown in Figure 1b. Based on the principle of stereology (Weibel, 1969), SSA (m^2/g) was then the product of a bias correction factor of $4/\pi$, bulk rock density (measured as 2.11 g/cm^3), and perimeter density. Because of the resolution difference between the BET measurement and SEM imaging, a roughness correction factor (Table 2) needs to be applied to match these two independent SSA measurements.

In this study, however, we are more interested in obtaining the SSA of individual minerals, in particular the SSA of individual minerals exposed to pore space, which we define as the accessible surface area. In principle, the global surface area is the sum of individual mineral accessible surface areas. To obtain the accessible surface area of individual minerals from the SEM-EDS image, we first calculated the perimeter density of individual minerals and then excluded the contact surface area between mineral grains. However, because of the

lower resolution (2.4 μm) and the limitation of the counting method employed on the SEM-EDS image, we need to down-scale the SEM-EDS image to the SEM-BSE image size, such that we take advantage of the high-resolution SEM-BSE image as well as the constrain of the BET measurement. To do that, it is necessary to apply a scaling factor (SF) to account for the differences between the two binary images, i.e., between the SEM-BSE and SEM-EDS images. To estimate this SF, minerals were grouped into three types: (i) minerals with fully filled grains, such as quartz, dolomite, K-feldspar, and ilmanite; (ii) minerals with partially filled grains, such as muscovite; (iii) minerals with poorly filled grains, such as Kaolinite. For each group, we selected 5-10 typical locations and calculated area fractions and perimeters of individual minerals for the two binary images. The SF was estimated using ratios of area fractions and of perimeters, as listed in Table 2. The volume fractions, listed in Table 1, were then obtained based on the principle of stereology (Weibel, 1969).
After applying the roughness correction, the perimeter density and the accessible perimeter density of individual minerals was obtained. Similar to the above approach to obtain SSA, the accessible SSA of individual minerals was calculated according to the principle of stereology (Weibel, 1969). The difference is that, instead of using bulk solid density, we use individual mineral densities (Table 1) to calculate the SSA and the accessible surface area of individual minerals. The results are listed in Table 2.

3. RESULTS AND DISCUSSION

3.1 Porosity and PSD

We measured the diameter and the length of the cylindrical rock sample with a Vernier calliper. From the measured diameter of 25.4±0.1 mm and the measured length of 39.0±0.1 mm, we obtained a sample volume of 19.7±0.1 ml. The sample solid volume of 15.441±0.004 ml was measured with a Helium pycnometer. We calculated a porosity of 21.9±0.4 %.
Figure 3 shows PSD from mercury intrusion measurements and from calculations on SEM image and 3D CT data. We smoothed the mercury porosimetry raw data (gray solid line) with a 10-ponit running averaging filter (to obtain the blue solid line). The mercury porosimetry results show a peak at a pore (throat) size of 15 μm in the range of 0.01 – 100 μm. SEM image analysis shows a peak at a pore size of 30 μm in the range of 1.2 – 80 μm. In addition to image resolution issues, the discrepancies between the curves is very likely introduced by the difference in measuring principles employed by these two methods, i.e., the mercury injection method better reflects the pore throat size, while the image analysis method is more sensitive to the total pore area. The PSD results are also partially confirmed by the 3D micro CT analysis. Due to the limitation of current computational resources, the resolution of the 3D CT image was up-scaled to 19.5 μm. For this resolution, most pores have been filtered-out so that only ~16% (relatively large) pores remain. The PSD from 3D CT data for pores bigger than 39 μm is shown as a black, dashed line in Figure 3, showing that the results from the analysis of 3D CT data match well with results from the analysis of 2D SEM data. This strongly suggests that the stereological method, used in this study, is valid. However, further analysis of smaller pore sizes is required.

3.2 Specific surface areas (SSA)

The bulk mass-specific surface area (SSA) of 1.447 m^2/g was determined by BET measurements, employing a 5-point-constrained line with a correlation coefficient of 0.99995. The stereological analysis of the SEM-BSE image (Figure 1b) yields a bulk SSA value of 0.031 m^2/g. After applying a resolution correction to the SEM-EDS image, the relative difference of the perimeter density, compared to the BSE image, was reduced from 40.0% to 2.9%, so that the stereological analysis yields a bulk SSA value of 0.032 m^2/g. After the roughness correction for individual minerals with their own scaling factors (SFs), shown in Table 2, the SSA of individual minerals is at a reasonable value, compared to literature values. The bulk SSA, i.e., the overall accessible SSA of all minerals, is then calculated as 1.441 m^2/g. This agrees well with the bulk BET measurement (1.447 m^2/g).

The volume fractions calculated from the extracted mineral maps are in very good agreement with the XRD and XRF results (Table 1). The accessible surface areas and their proportion before and after the correction are listed in Table 2. This suggests that the clay mineral kaolinite contributes more than 85% to the accessible surface area.

Our results suggest that lower and upper bounds for the accessible surface area could be determined, using the resolution correction and the roughness correction, respectively. We suggest that the resolution correction alone leads to an underestimation of the accessible surface area, resulting in a lower bound. In contrast, the roughness correction likely results in an overestimation of the accessible surface area, which would constitute an upper bound. We also note that the mineral accessible surface area, as defined in this paper (i.e., the surface area exposed to the pore space), does not account for the effective in-situ fluid accessibility during fluid flow. Therefore, further analyses of the accessible surface area are needed for our later flow-through experiments and pore-scale, reactive fluid flow simulations.

CONCLUSION

We have quantified the porosity and the PSD of rock samples, employing Helium pycnometry and Hg porosimetry, respectively. Rock compositions were determined by a combination of XRF, XRD, and SEM-EDS, which are later geometrically mapped onto 2D images, derived from SEM-BSE images. The stereological method used in this study is validated by comparing the mineral volume fraction, porosity, and PSD results from image processing and from laboratory measurements. Normalization of stereological specific surface area (SSA) to BET measurements of SSA yields roughness corrections of individual minerals. Our results indicate that image processing, combined with laboratory analyses, is a promising method to quantify a porous medium's reactive surface area.

ACKNOWLEDGEMENTS

This work is supported by a European project, entitled "Demonstration of soft stimulation treatments of geothermal reservoirs" (DESTRESS), funded by European Union's Horizon 2020 research and innovation programme under the grant agreement No.691728. The rock sample is provided by Geoterma, a Lithuanian geothermal energy company.

REFERENCES

1. Althaus, E, Edmunds, W.M., 1987, Geochemical research in relation to hot dry rock geothermal systems. Geothermics: 16, 451-458.
2. Beckingham, L.E., Mitnick, E.H., Steefel, C.L., et al., 2016, Evaluation of mineral reactive surface area estimates for prediction of reactivity of a multi-mineral sediment. Geochimica et Cosmochimica Acta: 188, 310-329.
3. Cai, R., Lindquist, W.B., Um, W., et al., 2009, Tomographic analysis of reactive flow induced pore structure changes in column experiments. Advances in Water Resources: 32, 1396–1403.
4. Cheshire, M.C., Stack, A.G., Carey, J.W., et al., 2017, Wellbore Cement Porosity Evolution in Response to Mineral Alteration during CO2 Flooding. Environmental Science & Technology: 51, 692-698.
5. Feng, G.H., Xu, T.F., Zhu, H.X., 2016, Dynamics of fluid and heat flow in a CO2-based injection-production geothermal system. Journal of Groundwater Science and Engineering: 4, 377-388.
6. Gaus, I., 2010, Role and impact of CO2–rock interactions during CO2 storage in sedimentary rocks. International Journal of Greenhouse Gas Control: 4, 73–89.
7. Hildebrand, T., Ruegsegger, P., 1997, A new method for the model-independent assessment of thickness in three-dimensional images. Journal of Microscopy: 185, 67–75.
8. Landrot, G., Ajo-Franklin, J.B., Yang, L., et al., 2012, Measurement of accessible reactive surface area in a sandstone, with application to CO2 mineralization. Chemical Geology: 318-319, 113-125.
9. Li, L., Peters, C.A., Celia, M.A., 2006, Upscaling geochemical reaction rates using pore-scale network modelling. Advances in Water Resources: 29, 1351–1370.
10. Luhmann, A.J., Kong, X.Z., Tutolo, B.M., et al., 2014, Experimental dissolution of dolomite by CO2-charged brine at 100 °C and 150 bar: Evolution of porosity, permeability, and reactive surface area. Chemical Geology: 380, 145-160.
11. Nogues, J.P., Fitts, J.P., Celia, M.A., et al., 2013, Permeability evolution due to dissolution and precipitation of carbonates using reactive transport modeling in pore networks. Water Resources Research: 49, 6006-6021.
12. Pandey, S.N., Chaudhuri, A., Rajaram, H., et al., 2015, Fracture transmissivity evolution due to silica dissolution/precipitation during geothermal heat extraction. Geothermics: 57, 111–126.
13. Peters, C.A., 2009, Accessibilities of reactive minerals in consolidated sedimentary rock: An imaging study of three sandstones. Chemical Geology: 265, 198-208.
14. Rasteniene, V., Puronas, V., 2005, Geothermal Atlas of Lithuania. Proceedings World Geothermal Congress 2005, Antalya, Turkey.
15. Voskov, D.V., Henley, H., Lucia, A., 2017, Fully compositional multi-scale reservoir simulation of various CO2 sequestration mechanisms. Computers & Chemical Engineering: 96, 183-195.
16. Weibel, E.R., 1969, Stereological Principles for Morphometry in Electron Microscopic Cytology. International Review of Cytology: 26, 235-302.

17. Xu, T.F., Apps, J.A., Pruess, K., 2003, Reactive geochemical transport simulation to study mineral trapping for CO2 disposal in deep arenaceous formations. Journal of Geophysical Research-Solid Earth: 108, Issue B2.
18. Yasuhara, H., Kinoshita, N., Lee, D.S., 2017, Evolution of mechanical and hydraulic properties in sandstone induced by simulated mineral trapping of CO2 geo-sequestration. International Journal of Greenhouse Gas Control: 56, 155-164.

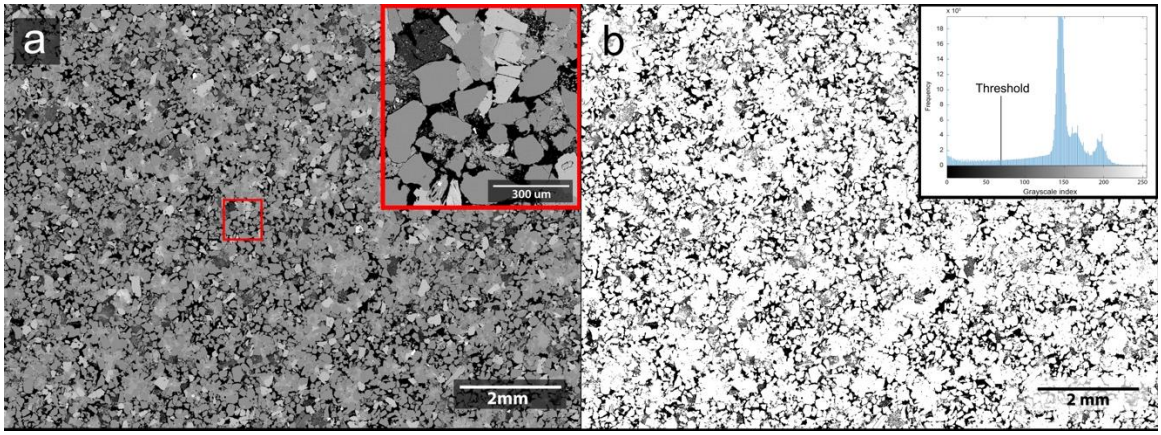

Figure 1: Analysis of the SEM-BSE image: (a) grayscale SEM-BSE image with a resolution of 1.2 µm, enlarged by a factor of 5 (inset in the right-upper corner) of the red square; (b) the corresponding binary image (black represents pores and white represents solid) with the inset showing a gray-value histogram and the applied threshold.

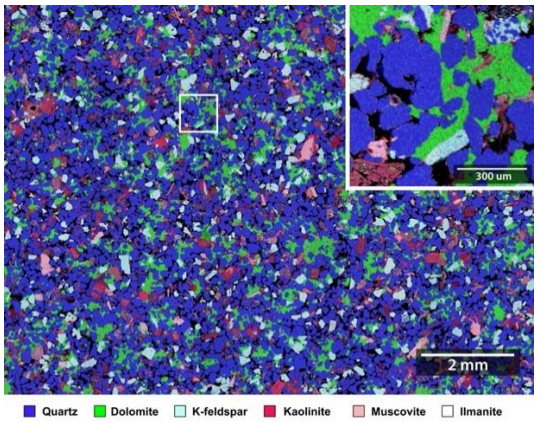

Figure 2: Mineral distribution of the SEM-EDS image with a resolution of 2.4 µm. Minerals are colour-coded as indicated at the bottom of the image.

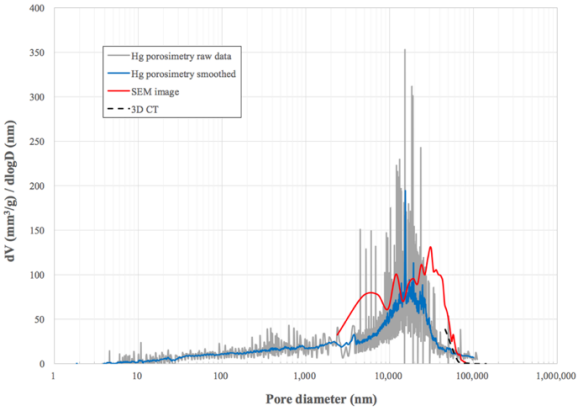

Figure 3: Comparison of PSDs obtained from mercury intrusion porosimetry, SEM image analysis, and analysis of 3D CT data.

Table 1: Minerals and their chemical formula, identified using a combined XRF+XRD method and SEM image processing. The mineral densities are from the engineering toolbox: http://www.engineeringtoolbox.com/mineral-density-d_1555.html

Mineral	Average chemical formula	Density g/cm^3	XRF+XRD vol.%	SEM vol. %
Quartz (Qtz)	SiO_2	2.62	47.65	45.53
Dolomite (Dol)	$CaMg_{0.77}Fe_{0.23}(CO3)_2$	2.84	12.36	12.22
K-feldspar (Ksp)	$KAlSiO_3$	2.56	11.82	9.93
Muscovite (Mu)	$K_{0.85}Na_{0.15}Al_2(AlSi_3O_{10})(OH)_2$	2.82	5.38	4.76
Kaolinite (Kln)	$Al_{1.9}Si_{2.1}O_5(OH)_4$	2.60	0.91	5.64
Ilmanite (Ilm)	$Fe_2Ti_5O_{12}$	4.72	0.23	0.27

Table 2: Scaling corrections for mineral area fractions (AF), perimeter densities (PD), and specific surface areas (SSA), based on SEM-BSE image analysis and literature BET values: quartz (Tester et al., 1993; Navarre-Sitchler et al., 2013), dolomite (Pokrovsky et al., 2005; Zhang et al., 2014; Zhang et al., 2015), K-feldspar (Stillings and Bratley, 1995; Richter et al., 2016), muscovite (Lin and Clemency, 1981; Kalinowski and Schweda, 1996; Richter et al., 2016), kaolinite (Wieland and Stumm, 1992; Devidal et al., 1997; Dawodu and Akpomie, 2014; Hai et al., 2015; Tan et al., 2017). Mineral abbreviations are listed in Table 1.

	Pore	Qtz	Dol	Ksp	Mu	Kln	Ilm	Total
EDS AF %	21.64	44.82	12.03	9.77	4.88	6.29	0.27	99.7
EDS accessible PD $\mu m/\mu m^2$		18382.6	1605.5	2181	1767.8	6875.4	242.1	31054.5
Resolution correction based on BSE image (BSE PD: 51567.3 $\mu m/\mu m^2$)								
SF applied to AF		1.02	1.02	1.02	0.98	0.9	1.02	
Res. corrected AF %	21.65	45.53	12.22	9.93	4.76	5.64	0.27	100
SF applied to PD		1.3	1.3	1.3	1.94	2.98	1.3	
Res. corrected accessible PD $\mu m/\mu m^2$		23897.4	2087.2	2835.3	3429.5	20488.8	314.7	53052.9
Roughness correction based on literature BET values of pure mineral (our bulk BET result: 1.447 m^2/g)								
Res. corrected accessible SSA m^2/g		0.040	0.037	0.039	0.089	0.230	0.052	0.03
Accessible SSA proportion %		45.05	3.93	5.34	6.47	38.62	0.59	
SSA from BET (Lit.)		0.02-0.55	0.07-1.96	0.08-0.25	0.66-5.53	13.2-78.0		
SF applied to SSA		5	50	5	50	100	25	
Rou. corrected accessible SSA m^2/g		0.20	1.87	0.19	4.47	23.04	1.29	1.441
Accessible SSA proportion %		5.00	4.37	0.59	3.59	85.79	0.66	